Aero-Optical Analysis of Species-Mismatched Supersonic Mixing Layers

Roberto Torres *, Pedro Castillo† and Andreas Gross‡
New Mexico State University, Las Cruces, NM 88003

Aaron Fassler§, Sergey Leonov¶ and Stanislav Gordeyev‖
University of Notre Dame, Notre Dame, IN 46556

During hypersonic flight, tangential cooling films blown over optical windows can protect them from damaging thermal effects from upstream hot turbulent boundary layers. As the cooling flow mixes with the freestream air, it creates a turbulent mixing layer, and a balance has to be struck between the cooling effectiveness and the resulting optical distortions. Optical distortions arise from density variations due to both the formation of coherent flow structures inside the mixing turbulent flow and the mixing process between generally different densities of the freestream flow and the cooling flow. To investigate these effects, wall-modeled large-eddy simulations of turbulent mixing layer flows over an optical window at a supersonic freestream speed of Mach 2 with carbon dioxide and helium as a working gas for the cooling film were carried out. The stagnation temperature of the freestream flow was varied between 300 K and 650 K. The conditions for the simulations match those of complimentary experiments. Differences between the velocities in the freestream flow and the cooling film, and density gradients across the mixing flow were found to affect the mixing layer turbulence and the production of baroclinic torque vorticity. The density fluctuations across the boundary layer feed directly into the optical path distortion. A density-based proper orthogonal decomposition reveals the presence of coherent structures that contribute to the optically aberrating distortions.

Nomenclature

*Graduate Research Assistant, Mechanical and Aerospace Engineering Department. AIAA Member.
†Graduate Research Assistant, Mechanical and Aerospace Engineering Department. AIAA Member.
‡Professor, Mechanical and Aerospace Engineering Department. AIAA Associate Fellow.
§Graduate Research Assistant, Aerospace and Mechanical Engineering Department. AIAA Member.
¶Research Professor, Aerospace and Mechanical Engineering Department. AIAA Associate Fellow.
‖Associate Professor, Aerospace and Mechanical Engineering Department. AIAA Associate Fellow.

This material is based on work originally presented as AIAA Paper 2025-2767, at the AIAA SCITECH 2025 Forum, 6-10 January 2025, Orlando, FL. doi: https://doi.org/10.2514/6.2025-2767

A	=	Area
a	=	Time coefficient
c	=	Mass fraction
c_f	=	Skin-friction coefficient
D	=	Mass diffusion coefficient
Ec	=	Eckert number
h	=	Specific enthalpy, nozzle exit height
H_i	=	Incompressible shape factor
k	=	Thermal conductivity
K_{GD}	=	Gladstone-Dale constant
L	=	Length
M	=	Mach number
n	=	Index of refraction
OPD	=	Optical path difference
OPL	=	Optical path length
Pr	=	Prandtl number
q	=	Heat flux
Q	=	Vortex identification criterion
R	=	Gas constant
Re	=	Reynolds number
r	=	Velocity ratio
s	=	Density ratio
S	=	Strain rate tensor
Sc	=	Schmidt number
t	=	Time
T	=	Temperature
u	=	Specific internal energy
u, v, w	=	Velocity in x, y, and z-direction
x, y, z	=	Cartesian coordinates
y	=	Mole fraction, wall distance
γ	=	Ratio of specific heats
δ	=	Boundary layer thickness

δ_{ij} = Kronecker symbol

δ^* = Displacement thickness

δ_Ω = Vorticity thickness

Δ = Grid length scale

θ = Momentum thickness

λ = Normalized velocity difference

μ = Dynamic viscosity

ρ = Density

τ = Shear stress, sub-grid stress

Φ = Normalized cumulative RMS OPD

Subscripts and Superscripts

0 = Stagnation condition

∞ = Freestream condition

in = Inflow condition

out = Outflow condition

ref = Reference

rms = Root-mean-square

s = Species

T = Turbulent

VD = Van Driest transformed

w = Wall condition

$+$ = In wall units

I. Introduction

Supersonic and hypersonic vehicles encounter unique challenges due to the extreme operational environment, such as shock waves and high heat loads. Optical sensors are required for navigation, communication and other mission critical tasks. These sensors are located behind optical windows that need to be actively cooled. Yi et al. [1] provide a review of aero-optical effects in hypersonic flight. In the infrared band relevant to optical seekers, infrared radiation from the optical window, shockwaves, and gas radiation all cause optical distortions that reduce the signal-to-noise ratio. The situation is aggravated by a reduction of the optical transmittance of the window and thermal stresses due to heating. A practical solution to the cooling problem is the injection of a secondary cooling film flow in the tangential direction over the window. The mixing layer that is formed by the outer boundary layer and the cooling film is highly

turbulent and exhibits strong density fluctuations. As the index of refraction is directly related to the density, optical beams passing through such flow regions are degraded.

The effect of the density ratio on the evolution of large-scale coherent flow structures for turbulent shear layers was investigated by Brown and Roshko [2]. Papamoschou and Roshko [3] introduced a convective Mach number that collapses the growth rate of compressible mixing layers and found that the growth rate decreases rapidly with increasing Mach number. The reduction of the growth rate with Mach number has later been reported by multiple other investigators [4–8]. Measurements for compressible mixing layers were carried out by Goebel and Dutton [9], Zhao et al. [10], Tan et al. [11], among others. Already in the 1970s, Goldstein et al. [12] investigated supersonic film cooling with gases such as air, freon, helium, nitrogen, and hydrogen, and put forward a relationship for the cooling film efficiency. Majeski and Weatherford [13] proposed another model for predicting the cooling film effectiveness for planar optical windows. Richards and Stollery [14] investigated laminar film cooling in a hypersonic gun tunnel. Out of a number of cooling film gases, they determined that hydrogen provided the most effective cooling. Kwok et al. [15] compared supersonic helium and air cooling film flows and found a much faster mixing for the former, which they attributed to the larger velocity and density gradients across the mixing layer. Juhany et al. [16] investigated Mach 1.2 to 2.2 air and helium cooling film flows in a Mach 2.4 freestream, where helium provided better cooling. The cooling film effectiveness improved with increasing cooling mass flow rate and Mach number. Auvity et al. [17] considered a helium cooling film under a Mach 8 boundary layer and found streamwise vortices downstream of the injection slot which they speculated to be due to centrifugal instability. Konopka et al. [18] performed large-eddy simulations (LES) of a hydrogen and helium Mach 1.3 cooling film flow for a Mach 2.44 turbulent boundary layer. For the former, the cooling was 14% more effective at a 60% lower mass flow rate. Peter and Kloker [19] employed direct numerical simulations (DNS) for investigating the interaction of a Mach 1.8 laminar helium cooling film with a Mach 3.3 flat plate water steam boundary layer. As the cooling film blowing ratio (defined by the streamwise momentum) was increased from 0.33 to 1, the mixing layer moved away from the wall, the mixing layer turbulence kinetic energy decreased, and the cooling film performance improved. Mi et al. [20] investigated supersonic nitrogen film cooling of a window in high-enthalpy Mach 9 flow for a blunt cone geometry. They varied the jet pressure ratio and slot height. Effective cooling was obtained when the jet exit pressure was matched to the freestream pressure. They proposed a scaling law for the cooling efficiency based on the blowing ratio, slot height, and streamwise coordinate and employed planar laser scattering and schlieren to visualize the cooling film. Sun et al. [21] showed that an optimum nozzle pressure ratio (NPR) exists where the cooling film remains effective over the longest downstream distance for a given cooling mass flow. Decreasing the cooling film thickness and increasing the cooling film Mach number can improve the cooling film effectiveness. Sun et al. [22] performed Reynolds-averaged Navier-Stokes calculations of a blunt fin circular cone with optical window and Mach 2.43 air cooling film and compared their results with Mach 7.1 experiments. With increasing NPR, the cooling mass flow increased and the cooling film remained effective over a longer downstream distance. Planar laser scattering

visualizations by Xia et al. [23] revealed that micro vortex generators (MVGs) can suppress the shedding of large-scale spanwise shear-layer structures. Sun et al. [24] demonstrated that MVGs reduce the optical window heat flux by over 30%.

A considerable body of recent literature is dedicated to the optical path distortions for cooling film flows. Ayyalasomayajula et al. [25] proposed that wavefront phase aberrations and root-mean-square optical path differences (OPD_{rms}) result mainly from shocklets. Su [26] investigated supersonic air, helium, and CO_2 cooling film flows in a Mach 2 boundary layer. Linear stability analyses revealed a narrower unstable frequency range for helium with overall lower frequencies and smaller disturbance amplitudes compared to other gases. The optical path distortion for helium was also found to be lower than for air and CO_2. Ding et al. [27] performed wavefront measurements for a supersonic cooling film at different density ratios and found an exponential relationship between the Strehl ratio and the optical path distortions per wavelength. Guo et al. [28] combined LES of a mixing layer over an optical window with ray tracing simulations to determine the location and incidence angle for the optical beam that yielded the lowest distortions. Yao et al. [29] performed experiments with supersonic air and CO_2 cooling film. The optical distortions and condensation of the cooling gas increased linearly with NPR for air and exponentially for CO_2 with overall larger optical distortions for CO_2. Ding et al. [30] showed that MVGs upstream of the window can significantly reduce the optical distortions. A recent simulation by Patel et al. [31] revealed the impact of coherent structures on the density fluctuations. Researchers at the University of Notre Dame (ND) investigated the optical distortions for temperature- and species-mismatched cooling films [32–35] in the SBR-50 facility [36]. They considered canonical cooling film flows over an optical window that was recessed into a cavity. In addition of using air as a coolant, species-mismatched cases with CO_2 and helium as cooling gases were also investigated. The cavity was defined by a backward-facing step that was followed by a compression ramp. The coolant gas was injected from the base of the backward facing step. While the jet cools the window, it introduces optical distortions as a result of the velocity and density mismatch with the freestream and resulting instabilities that lead to the development of coherent structures within the mixing layer. An optimal design maximizes cooling while minimizing optical distortions. Based on the experiment, ND researchers developed a new scaling law for aero-optical distortions at mismatched temperatures. Torres Andrade et al. [37] performed wall-modeled LES (WMLES) of the temperature-mismatched experiments and employed proper orthogonal decomposition (POD) [38, 39] to isolate coherent flow structures. The simulations showed that with increasing freestream total temperature, the reduction in freestream density diminishes the contribution of the incoming turbulent boundary layer to the OPD. At the same time, the velocity difference and turbulence levels across the mixing layer are increased, resulting in a stronger mixing layer contribution to the OPD. As a result of these competing mechanisms, the levels of aero-optical distortions are not linearly dependent on the freestream total temperature.

This paper reports on WMLES of species-mismatched mixing layers with CO_2 and helium as cooling film gases, designed to match the conditions of complimentary experiments at ND. For completeness, some details of the experiments

are presented and discussed. Several different cases are defined, the numerical method is briefly summarized, the subgrid and wall-modeling are discussed, curve fits for the thermo-physical properties are presented, and the computational grid and boundary conditions are introduced. In the following sections, instantaneous flow visualizations are presented and the mixing layer mean flow, turbulent statistics, and root-mean-square (RMS) density fluctuations are compared. Profiles of the cooling gas concentration and baroclinic torque provide additional insight into the cooling film behavior. The time-averaged levels of the aero-optical distortions are computed and compared with the experiments. A POD with density-based kernel is employed to isolate coherent mixing layer structures and their contribution to the optical distortions is quantified. The paper concludes with a brief discussion of the results.

II. Methodology

A. Experimental Setup

A detailed description of the experiments can be found in Refs. [32–35], so only essential details relevant to the simulations are provided here. The experiments were carried out in the SRB-50 tri-sonic wind tunnel (TWT) at the University of Notre Dame (ND). The tunnel operating gas is air and the test section height and width are $78.4mm \times 76.2mm$. The freestream Mach number in the experiments was $M_\infty = 2$, the total pressure was maintained at $p_0 = 2.6 \times 10^5 Pa$, and the total temperature was varied between $T_0 = 295K$ and $750K$. The boundary layer thickness and momentum thickness for $T_0 = 295K$ were estimated to be $\delta = 3.2mm$ and $\theta = 0.275mm$, respectively. An optical window was mounted inside the test section bottom wall (Fig. 1). The window was recessed by 5 mm and a secondary cooling film (air, carbon dioxide, or helium) was injected through a two-dimensional nozzle to form a wall jet over the optical window. The cooling jet stagnation temperature was $\approx 295K$. In this paper, results for carbon dioxide and helium as secondary gas are presented. Results for air as secondary gas can found in Fassler et al. [32, 33] and Torres Andrade et al. [37]. Honeycomb flow straighteners in the nozzle inflow were used to improve the cooling jet flow uniformity. The nozzle inflow and outflow duct height were $h_{in} = 50.8mm$ and $h_{out} = 4mm$, respectively, and the nozzle width was $76mm$. A second optical window was placed on the opposite wall of the test section to create an optical path in the wall-normal direction for measuring the optical path distortion (OPD) of the flow over the recessed window on the bottom wall. The OPD measurements were performed with an Nd:YaG laser with a wavelength of 532 nm.

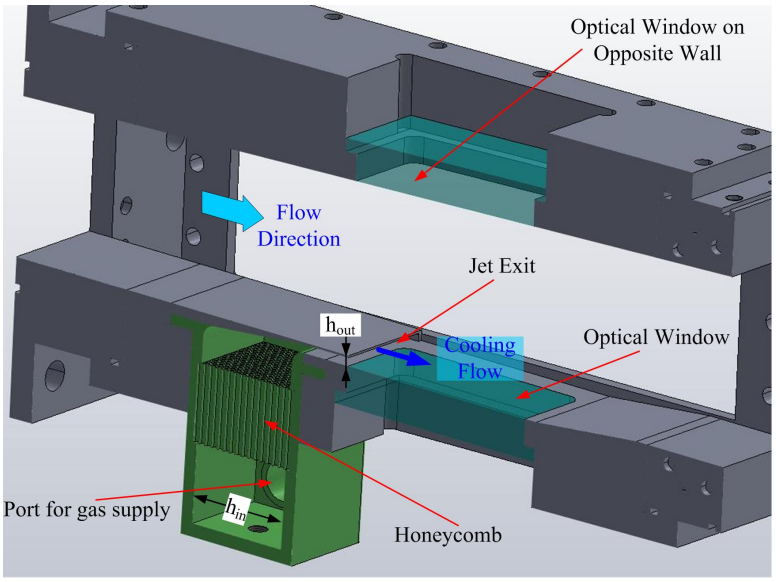

Fig. 1 Cut-out of test section, with major features labeled. Flow is from left to right.

B. Setup for Simulations

The present species-mismatched simulations are for air as freestream gas of the mixing flow. The freestream stagnation temperature is either $T_0 = 300K$ or $650K$. For the cooling gas, two gas species are considered, carbon dioxide (CO_2) and helium (He). The stagnation temperature of the cooling gas is kept the same and equals 300 K. The freestream properties for the cases are summarized in Tab. 1. The first number in the case descriptors references the freestream properties and the second number references the cooling gas with "1" for CO_2 and "2" for He.

Table 1 Freestream properties.

Cases	$T_0(K)$	$u_\infty(m/s)$	$T_\infty(K)$	$\rho_\infty(kg/m^3)$	$Re_{1m}(\times 10^6)$
T1S1, T1S2	300	517.8	166.7	0.6942	31.74
T2S1, T2S2	650	761.8	361.1	0.3206	11.51

Assuming a constant total enthalpy and isentropic flow, the nozzle inflow and outflow Mach number are related via,

$$\frac{A_{in}}{A_{out}} = 12.7 = \frac{M_{out}}{M_{in}} \left[\frac{1 + \frac{\gamma-1}{2} M_{in}^2}{1 + \frac{\gamma-1}{2} M_{out}^2} \right]^{\frac{\gamma+1}{2(\gamma-1)}}. \tag{1}$$

The static pressure at the nozzle exit was matched to the freestream pressure, $p_{out} = p_\infty = 33,229Pa$. From this, the nozzle inflow and outflow Mach number were determined. The cooling jet properties change depending on the gas species (carbon dioxide or helium), affecting the streamwise development of the mixing layer over the cavity and the

aero-optical distortions. The cooling film properties for the different cases are summarized in Tab. 2. In Tab. 3, the dimensionless nozzle outlet velocity and density, r and s, as well as the normalized velocity difference, λ, are compared with the experiment [34, 35]. The overall agreement is good.

Table 2 Cooling film properties.

Case	Cooling gas	$T_{out}(K)$	$u_{out}(m/s)$	$\rho_{out}(kg/m^3)$	γ	R $[J/kgK]$
T1S1	CO_2	282.1	172.6	0.6152	1.29	189.1
T2S1	CO_2	284.8	157.2	0.6284	1.29	189.1
T1S2	He	290.6	296.3	0.0546	1.66	2080
T2S2	He	290.5	301.4	0.0546	1.66	2080

Table 3 Comparison of cooling film properties at nozzle exit. Experiments by Fassler et al. [34, 35].

Case		$r = \frac{U_{out}}{U_\infty}$	$s = \frac{\rho_{out}}{\rho_\infty}$	$\lambda = \frac{U_\infty - U_{out}}{U_\infty + U_{out}} = \frac{1-r}{1+r}$.
T1S1	Exp.	0.33	0.85	0.50
	WMLES	0.3333	0.8862	0.5000
T2S1	Exp.	0.22	1.9	0.64
	WMLES	0.2063	1.960	0.6580
T1S2	Exp.	0.57	0.078	0.27
	WMLES	0.5612	0.0786	0.2811
T2S2	Exp.	0.39	0.17	0.44
	WMLES	0.3956	0.1703	0.4331

C. Numerical Method

The simulations were performed with a research computational fluid dynamics code [40, 41] that solves the filtered compressible Navier-Stokes equations, which were closed with a sub-grid stress model, in the finite-volume formulation. The convective fluxes were computed with the Lax-Friedrichs scheme (maximum eigenvalue over stencil width) and interpolated onto the cell faces with a ninth-order-accurate weighted essentially non-oscillatory scheme [42]. A fourth-order-accurate discretization was employed for the viscous terms. The governing equations were integrated in time with the second-order-accurate implicit trapezoidal rule. The species internal energy and enthalpy as well as

diffusion coefficients (viscosity, heat conduction, mass diffusion) were obtained from curve fits. Wilke's mixing law was applied to compute the mixture properties.

D. Non-Dimensionalization

For the simulations, all quantities were made dimensionless with their respective freestream values and an arbitrary reference length scale ($L_{ref} = 1m$). The freestream Mach number was $M_\infty = 2$ and the unit Reynolds number, Re_{1m}, is provided in Tab. 1. The laminar and turbulent Prandtl and Schmidt number were $Pr = 0.71$, $Pr_T = 0.9$, $Sc = 0.5$, and $Sc_T = 0.5$. In the following, only time is presented in dimensionless form, where one time unit corresponds to the time it takes for the freestream to travel one meter. The dimensional time can be obtained from the dimensionless time by multiplication with L_{ref}/u_∞.

E. Sub-Grid Stress Model

The wall-adapting local eddy-viscosity (WALE) model by Nicoud and Ducros [43] was employed for computing the sub-grid eddy viscosity,

$$\mu_T = \bar{\rho}(C_w\Delta)^2 \frac{(S_{ij}^d S_{ij}^d)^{3/2}}{(S_{ij}S_{ij})^{5/2} + (S_{ij}^d S_{ij}^d)^{5/4}}\,, \tag{2}$$

where

$$S_{ij}^d = \frac{1}{2}\left(g_{ij}^2 + g_{ji}^2\right) - \frac{1}{3}\delta_{ij}g_{kk}^2 \tag{3}$$

is the trace-less symmetric part of the square of the velocity gradient tensor and $g_{ij}^2 = g_{ik}g_{kj}$. The model constant, C_w, was taken as 0.325. The grid length-scale, Δ, was taken as the cubic root of the cell volume.

F. Sub-Grid Stress, Heat and Species Diffusion

The sub-grid stress tensor was modeled as

$$\rho\tau_{ij} = 2\mu_T\left(S_{ij} - \frac{1}{3}S_{kk}\delta_{ij}\right)\,. \tag{4}$$

The sub-grid heat flux was modeled as

$$q_i = -k\frac{\mu_T}{\mu}\frac{Pr}{Pr_T}\frac{\partial T}{\partial x_i}\,, \tag{5}$$

and the sub-grid mass diffusion was modeled as

$$j_{s,i} = -D_s\frac{\mu_T}{\mu}\frac{Sc}{Sc_T}\frac{\partial y_s}{\partial x_i}\,. \tag{6}$$

Here, k is the mixture heat conduction coefficient, μ is the mixture viscosity, D_s is the mass diffusion coefficient (for diffusion of species s into the mixture), and y_s are the mole fractions.

G. Wall-Modeling

To overcome the near-wall grid resolution requirement, which would otherwise make the LES prohibitively expensive, rather then resolving the near-wall region, ordinary differential equations for the species mole fractions, streamwise velocity, and temperature,

$$\frac{\partial}{\partial y}\left[\frac{D_s + D_{s,T}}{ReSc}\rho\frac{\partial y_s}{\partial y}\right] = 0\,, \tag{7}$$

$$\frac{\partial}{\partial y}\left[\frac{\mu + \mu_T}{Re}\frac{\partial u}{\partial y}\right] = 0\,, \tag{8}$$

$$\frac{\partial}{\partial y}\left[\frac{k + k_T}{RePrEc}\frac{\partial T}{\partial y} + \rho\sum_s \frac{D_s + D_{s,T}}{ReSc}h_s\frac{\partial y_s}{\partial y} + u\frac{\mu + \mu_T}{Re}u\frac{\partial u}{\partial y}\right] = 0\,, \tag{9}$$

were solved with a shooting method from the wall to a matching point (third cell of the wall). Here, h_s are the species enthalpies and $Ec = {u_\infty}^2/(c_{p,\infty}T_\infty)$ is the Eckert number. The wall model provides the wall mole fractions, shear stress, and wall temperature (for adiabatic wall).

H. Curve Fits for Thermo-Physical Properties

The viscosity and thermal conductivity were obtained from Sutherland's law,

$$\mu = \mu_0\left(\frac{T}{T_0}\right)^{3/2}\left(\frac{T_0 + S_\mu}{T + S_\mu}\right)\,, \tag{10}$$

$$k = k_0\left(\frac{T}{T_0}\right)^{3/2}\left(\frac{T_0 + S_k}{T + S_k}\right)\,, \tag{11}$$

with coefficients from Tab. 4. The relationships are plotted in Fig. 2 together with data obtained from CoolProp by Bell et al. [44]. Sutherland's law approximates the dynamic viscosity within 6%. The polynomials for the thermal conductivity are close to the reference data.

Table 4 Coefficients for Sutherland's law.

Gas	$T_0\ (K)$	$\mu_0\ (Ns/m^2)$	$S_\mu(K)$	$k_0\ (W/m/K)$	$S_k\ (K)$
Air	273	1.716×10^5	111	0.0241	194
CO_2	273	1.370×10^5	222	0.0146	1800
He	273	1.886×10^5	79.44	0.1476	80.51

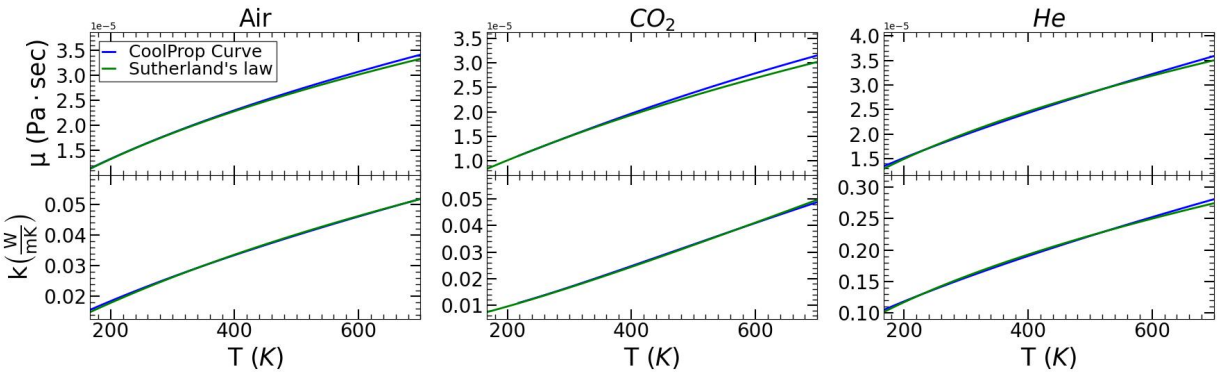

Fig. 2 Viscosity and thermal conductivity from CoolProp and Sutherland's law.

The specific enthalpy (h) and internal energy (u) were obtained from CoolProp for the expected temperature range of the simulations. These data, together with polynomial curve fits that were used in the simulations, are depicted in Fig. 3. The mass diffusion coefficients for CO_2 and He into air were obtained from Engineering ToolBox [45]. The data and polynomial curve fits for the simulations are shown in Fig. 4.

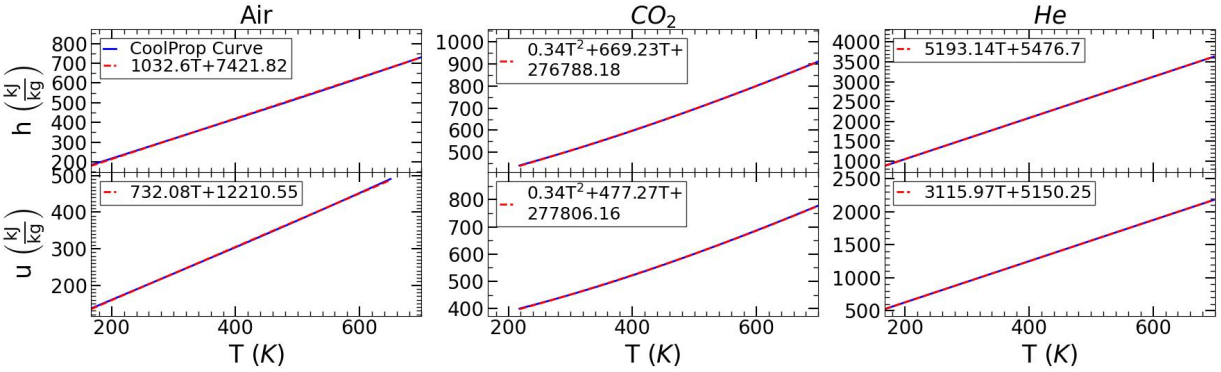

Fig. 3 Specific enthalpy and energy from CoolProp and polynomial curve fits.

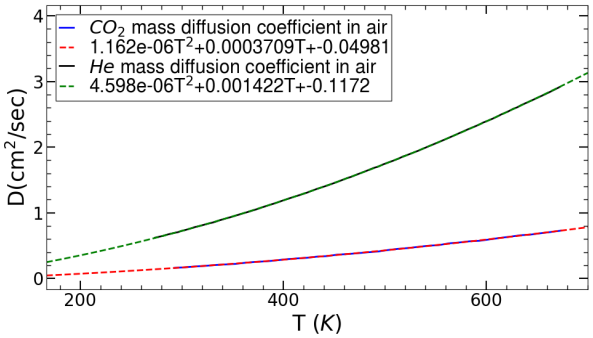

Fig. 4 Mass diffusion coefficient from Engineering Toolbox and polynomial curve fits.

I. Computational Grid

The grid for the present simulations is identical to that employed in the previous simulations by Torres Andrade et al. [37] of the ND experiments with temperature-mismatched air mixing layer. The grid is divided into three sub-domains or blocks and the origin of the coordinate system is at the lower left corner of the cavity (Fig. 5). Information about the blocks is provided in Tab. 5. Block 1 is rectangular and features a constant grid-line spacing in the streamwise and spanwise directions. Near the block 1 outflow, the streamwise grid-line spacing is reduced to resolve the corner flow. A wall-normal grid line spacing of $\Delta y/\delta = 0.02$ was employed between the wall and $y/\delta = 0.2$. Outside the near-wall region ($y/\delta > 0.2$), the wall-normal grid line stretching is initially 5% and then decreases away from the wall. Block 2 is mostly rectangular but features a $4deg$ compression ramp at the outflow. The height of the backward facing step is $h = 5mm$ and the compression ramp starts $x = 0.11m$. Streamwise grid refinement at the block 2 inflow is employed to resolve the rear side of the backward facing step. Downstream of the block 2 inflow, the wall-normal grid lines are redistributed to obtain a more balanced wall-normal grid line distribution. Similar to block 1, a layer with constant wall-normal grid distribution is employed at the wall. The streamwise grid line spacing is first constant and then increases near the outflow to dissipate flow structures. Block 3 (nozzle) was created with a Poisson grid generator [46]. For all three blocks, an equidistant grid line spacing was employed in the spanwise direction. Torres Andrade et al. [37] provide additional information about the grid (number of grid points across mixing layer, ratio of grid line spacing to Kolomogorov length scale) and demonstrate that the grid resolution is sufficient for WMLES.

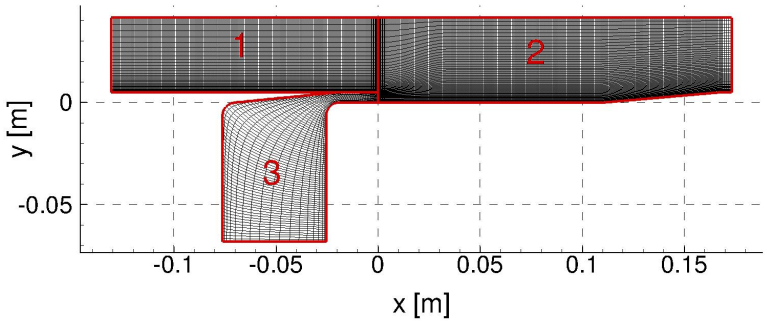

Fig. 5 Computational grid. For clarity, every other grid line is omitted in the streamwise and wall-normal directions for blocks 1 and 2.

Table 5 Domain size and number of cells per block.

Block	Domain size		Number of cells	Total number of cells
1 (Inflow)	$0.130m \times 0.03668m \times 0.013m$	$26h \times 7.33h \times 2.6h$	$512 \times 64 \times 160$	5.24×10^6
2 (Cavity)	$0.173m \times 0.04168m \times 0.013m$	$35.6h \times 8.33h \times 2.6h$	$666 \times 102 \times 160$	10.86×10^6
3 (Nozzle)	$0.0762m \times 0.073m \times 0.013m$	$15h \times 14.6h \times 2.6h$	$192 \times 38 \times 160$	1.16×10^6

J. Boundary Conditions

No-slip and no-penetration conditions were enforced at the walls. The walls were considered adiabatic and the species mass fraction gradients at the walls were set to zero. Dirichlet conditions were enforced at the inflow and Neumann conditions were applied at the outflow boundary. Characteristics-based boundary conditions [47] were employed at the freestream boundary. Flow periodicity was enforced in the spanwise direction. The rescaling and recycling method by Stolz and Adams [48] was employed to sustain a turbulent approach flow boundary layer. The recycling plane was at $x = -15.7mm$ and the block 1 inflow target momentum thickness Reynolds number was 9,000. More details about the rescaling and recycling method are provided in Torres Andrade et al. [37].

K. Computational Timestep and Time Interval for Computing Statistics

The computational timestep was $\Delta t = 0.0001$ for case T2S2 and $\Delta t = 0.0002$ for the three other cases. The time intervals for computing the time averages and statistical quantities was one.

L. Optical Path Length and Optical Path Difference

To investigate the optical aberrations, the density fields were first converted into index-of-refraction, n, fields via the linear Gladstone-Dale relation [49],

$$n(x, y, z, t) = 1 + K_{GD} \times \rho(x, y, x, t)\,, \tag{12}$$

where K_{GD} is the Gladstone-Dale constant. The Gladstone–Dale constant for gas mixes was mass-averaged [50],

$$K_{GD} = \sum c_s K_{GD,s}, \tag{13}$$

where $c_s = \rho_s/\rho$ are the mass fractions and $K_{GD,s}$ are the Gladstone-Dale constants of the individual species. Values of the Gladstone–Dale constants for the individual species at the wavelength of 532 nm [51–53], used in the presented simulations, are listed in Tab. 6.

Table 6 Gladstone-Dale constants at wavelength of 532 nm.

Species	$K_{GD}(m^3/kg)$
Air	2.27×10^{-4}
CO_2	2.29×10^{-4}
He	1.96×10^{-4}

Integration of the index-of-refraction from the wall to the freestream provides the optical path length,

$$OPL(x,z,t) = \int_0^y n(x,y,z,t)dy\,. \tag{14}$$

To be consistent with the analysis of the experimental data, the time-mean OPL is removed to obtain the optical path difference,

$$OPD(x,z,t) = OPL(x,z,t) - \overline{OPL(x,z,t)}\,, \tag{15}$$

where an overbar denotes time averaging. Finally, the overall level of aero-optical distortions, OPD_{rms}, defined as the time-averaged value of the spatial root-mean-square (RMS) of the OPD is calculated as

$$OPD_{rms} = \sqrt{\overline{\langle OPD^2(x,z,t)\rangle_{(x,z)}}}\,. \tag{16}$$

with angled brackets denoting the spatial averaging.

M. Proper Orthogonal Decomposition

The proper orthogonal decomposition (POD) by Lumley [38] is well suited for the analysis of turbulent flows. Typically, the computationally efficient "snapshot" method by Sirovich [39, 54] is employed. The POD provides a compact representation (least number of modes required) of unsteady flows. For the present work, the interest is on the optical distortions which are caused by density fluctuations. Therefore, a density-based POD kernel, $\rho_i\rho_j$, was chosen. The POD modes are orthogonal and sorted according to their respective energy content. The POD eigenvalue magnitudes are identical to the square of the density fluctuations of the respective modes. The instantaneous density field, $\rho(\mathbf{x},t)$, can be reconstructed from the time-coefficients, $a_i(t)$, and POD modes, $m_i(\mathbf{x})$, via

$$\rho(\mathbf{x},t) = \sum_i a_i(t)m_i(\mathbf{x})\,. \tag{17}$$

III. Results

A. Approach Boundary Layer

In Fig. 6, the van Driest transformed velocity,

$$u^{VD} = \int \sqrt{\frac{\rho}{\rho_w}} du^+, \tag{18}$$

is plotted versus the wall distance in wall units, y^+, for $x/h = -2.14$. The solid and dashed lines are for the resolved part and the dotted lines are for the modeled part (i.e., from wall model). As a reference, relationships for the viscous sublayer, $u^+ = y^+$, and the log-layer, $u^+ = 5 + (\ln y^+)/0.41$, (dotted and dashed black lines) are included. The log-layer slope is matched with good accuracy and the defect layer is well represented. The matching point (for the wall model) is near $y^+ = 160$ and well within the log-layer.

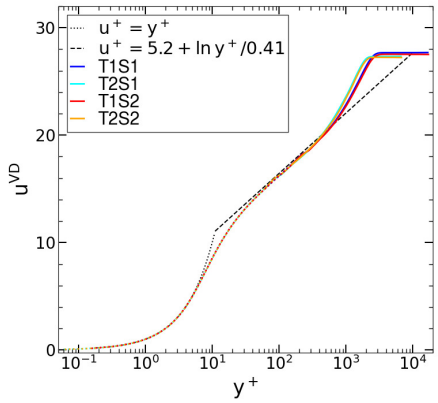

Fig. 6 Velocity profiles in wall units for x/h=-2.14 (·····, from wall model, ——, resolved).

B. Mixing Layer

Snapshots of the streamwise velocity, cooling gas mass fraction and density in Figs. 7, 8, and 9 reveal the turbulent nature of the approach boundary layer and mixing layer. Corresponding mean profiles are provided in Fig. 10. The approach boundary layer is noticeably thicker for the higher freestream stagnation temperature (see Fig. 10a). As the freestream stagnation temperature is raised, the freestream speed of sound and velocity increase, while the freestream Mach number remains constant (i.e., it is set by the wind tunnel nozzle area ratio). The isentropic exponent γ for CO_2 is different from He. As a result, for the same cooling jet nozzle geometry, the cooling jet is faster for He compared to CO_2 as also seen in Fig. 10a. In terms of velocity shear across the mixing layer, the cases can be sorted as T2S1 (highest shear), T1S1, T2S2, T1S2 (lowest shear). Figure 8 provides instantaneous visualizations of the species mass fractions. Compared to the CO_2 cases, for the He cases the cooling gas is mixing faster with the freestream air (also see

Fig. 10b). The freestream density decreases when the tunnel stagnation temperature is raised (Fig. 9). With increasing freestream total temperature, the freestream density drops. For cases T1S1 and T2S2, the cooling film and freestream density are similar (Fig. 10c). For case T2S1, the cooling film is denser than the freestream and for case T1S2, the freestream is denser than the cooling film. In terms of density difference across the mixing layer, the cases can be sorted as T1S2 (largest density difference), T2S1, T2S2, T1S1 (smallest density difference). As a final comment on the density profiles, for the high temperature cases (T2S1 and T2S2) the density decreases close to the wall. This effect is more pronounced for case T2S1.

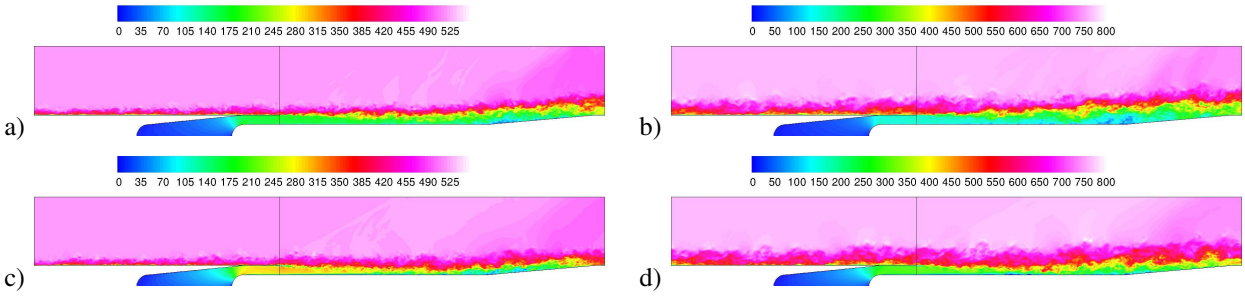

Fig. 7 Instantaneous streamwise velocity (in m/s) for a) T1S1, b) T2S1, c) T1S2 and d) T2S2.

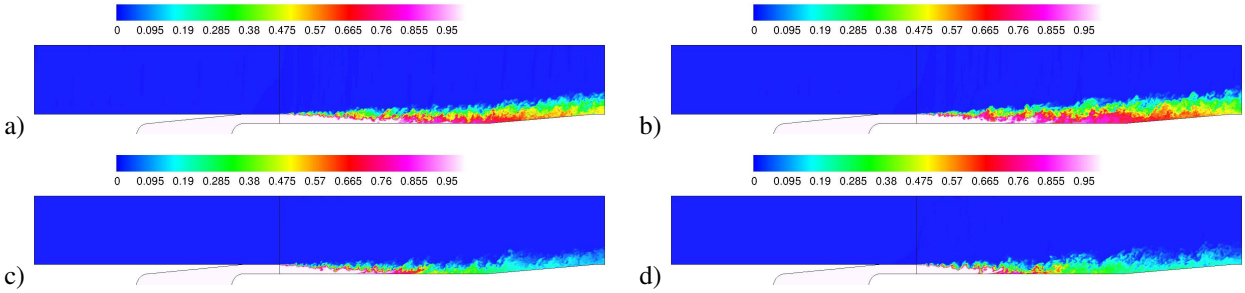

Fig. 8 Instantaneous cooling gas mass fraction for a) T1S1, b) T2S1, c) T1S2 and d) T2S2.

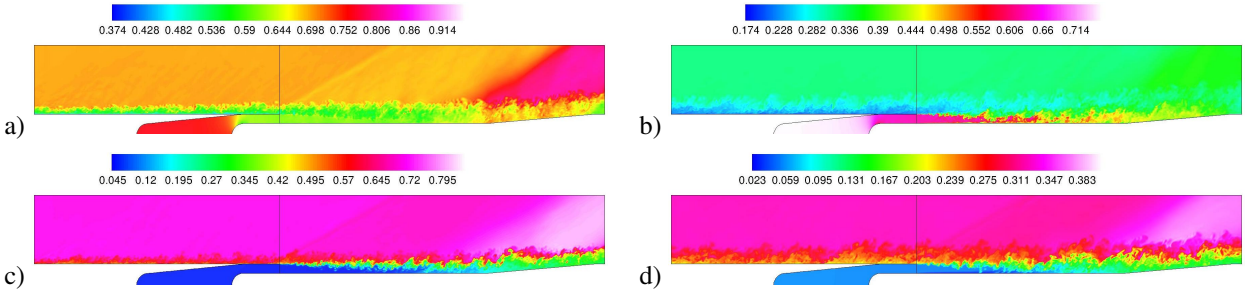

Fig. 9 Instantaneous density (in kg/m^3) for a) T1S1, b) T2S1, c) T1S2 and d) T2S2.

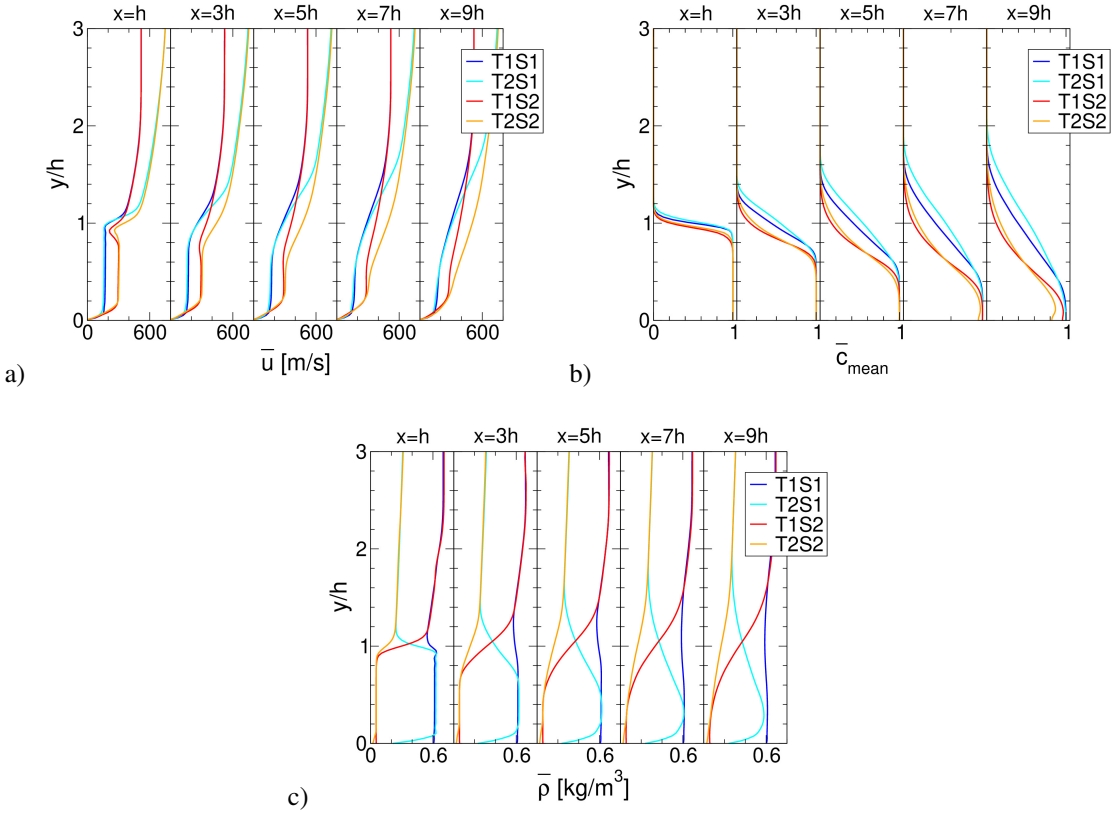

Fig. 10 Mean a) velocity, b) cooling gas mass fraction, and b) density profiles for x=(2n+1)h (n=0, 1, ... 4).

Distributions of the adiabatic wall temperature along the cavity bottom wall are provided in Fig. 11. Helium is a better cooling agent than carbon dioxide and maintains a lower adiabatic wall temperature for $T_0 = 650K$. For the cases with higher freestream total temperature (T2S1 and T2S2), the adiabatic wall temperature begins to rise more quickly near $x/h = 10$.

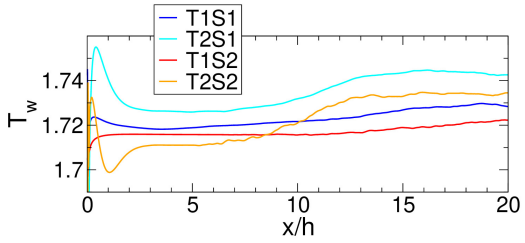

Fig. 11 Adiabatic wall temperature.

In Fig. 12a, the standard quantity to define the mixing layer thickness, the vorticity thickness,

$$\delta_\Omega = \frac{U_\infty - U_{out}}{\left(\frac{\partial U}{\partial y}\right)_{max}}, \tag{19}$$

is plotted versus the streamwise coordinate, measured from the nozzle outlet. The dotted lines are linear curve fits. In Fig. 12b, the mixing layer spreading rate is plotted against λ and compared with data from the literature [2, 55–58] and earlier WMLES with air cooling film [37]. Open symbols are used for the simulations. With increasing tunnel total temperature, the mixing layer spreads faster. The CO_2 cases are in good agreement with the reference data. The spreading rate for the helium cases is generally higher.

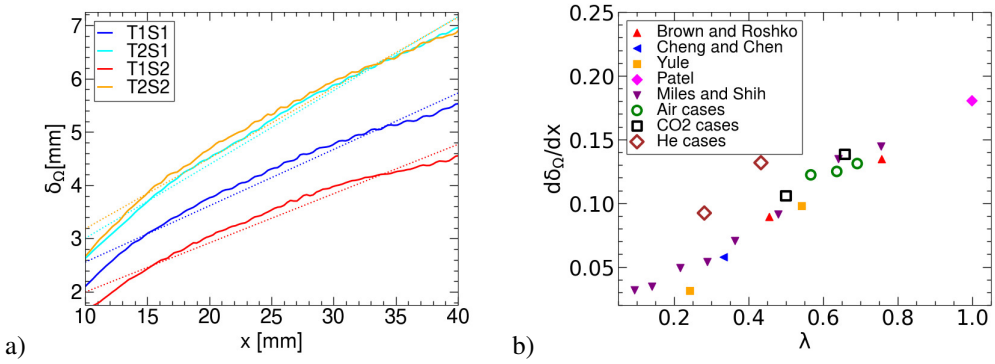

Fig. 12 a) Vorticity thickness (——) with linear fits (·····) and b) spreading rate.

The baroclinic torque, $(\nabla\rho\times\nabla p)/\rho^2$, shows up as production term in the vorticity transport equation. The barocylinc torque for the species-mismatched cases was computed over a time interval of 0.2. Figure 13 provides profiles of the absolute of the time mean baroclinic torque. Because of the low density of helium, the mean barocylinic is higher than for the CO_2 cases. For CO_2, the density difference across the mixing layer increases when T_0 is raised (see Fig. 10c), leading to an increase of the mean baroclinic torque.

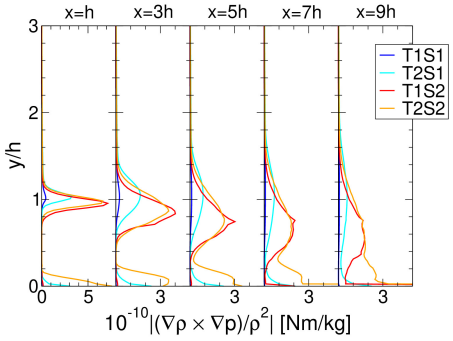

Fig. 13 Absolute baroclinic torque profiles for x=(2n+1)h (n=0, 1, ... 4).

Profiles of the turbulence kinetic energy (TKE) and turbulent shear stress are provided in Fig. 14. Turbulence production in the mixing layer is driven by velocity shear and baroclinic torque. For the CO_2 cases, the maxima of the TKE are near the inflection point of the velocity profiles (Fig. 10a). For the *He* cases, the TKE peaks are near the maxima of the baroclinic torque profiles (Fig. 13). The velocity difference across the mixing layer is largest for case

T2S1 (CO_2, $T_0 = 650K$) and this case exhibits the largest TKE and turbulent shear stress. For helium, the mixing layer is overall less turbulent and the turbulence decays more quickly compared to CO_2.

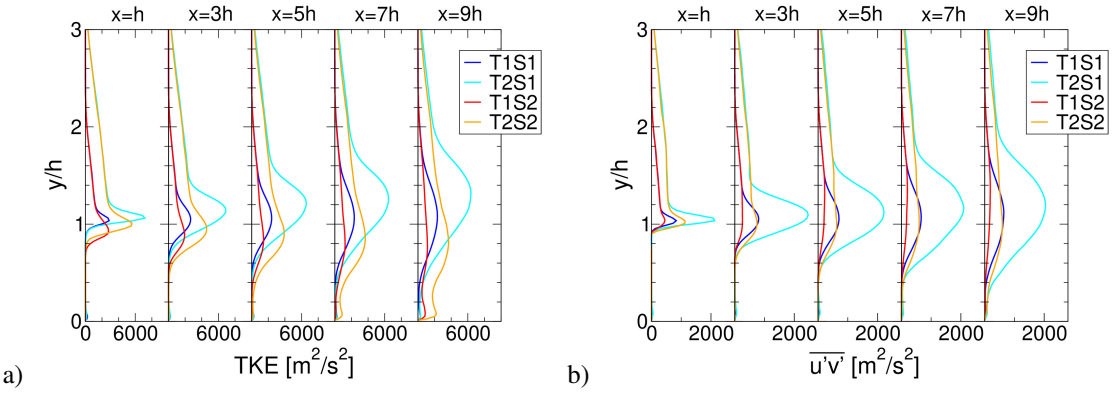

Fig. 14 a) Turbulence kinetic energy and b) turbulent shear stress profiles for x=(2n+1)h (n=0, 1, ... 4).

Profiles of the RMS fluctuations of the cooling gas mass fraction are provided in Figs. 15. For case T2S1, in agreement with the large TKE at the mixing layer edge, the RMS fluctuations spread farther into the freestream. For the *He* cases, the RMS fluctuation peaks are closer to the wall in agreement with the higher near-wall baroclinic torque.

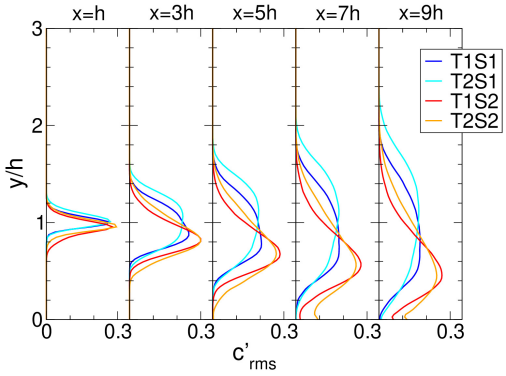

Fig. 15 Cooling gas mass fraction RMS fluctuation profiles for x=(2n+1)h (n=0, 1, ... 4).

Profiles of the density RMS fluctuations are shown in Fig. 16. A differentiation can be made between the approach boundary layer ($1 \leq y/h \leq 3$) and mixing layer ($y/h \approx 1$) density fluctuations. The boundary layer RMS density fluctuations are generally subdominant to the mixing layer fluctuations and higher for the low-temperature cases (which have a larger density gradient across the approach boundary layer). For case T1S1 (CO_2, $T_0 = 300K$), the mixing layer velocity and density gradients are low and, as a result, the mixing layer turbulent shear-stress (Fig. 14b) and RMS density fluctuations (Fig. 16) are small. The mixing layer RMS density fluctuations are largest for cases T2S1 and T1S2 (Fig. 16). This is explained by the large velocity gradient across the mixing layer for case T2S1 (see Fig. 10a), which

leads to strong turbulent mixing (see Fig. 14), and by the large density gradient across the mixing layer for case T1S2 (see Fig. 10c). The secondary near-wall peak of the density fluctuations for case T2S1 is explained by the large near-wall density gradient (see Fig. 10c). Benign velocity and density gradients cause mild RMS density fluctuations for case T2S2 ($He, T_0 = 650K$).

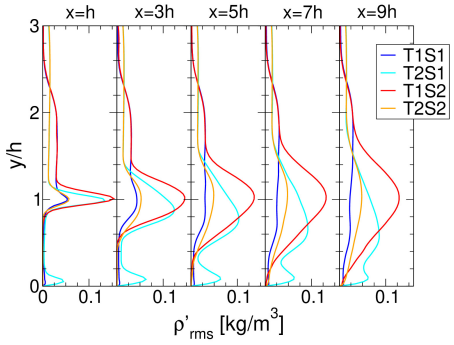

Fig. 16 Density RMS fluctuation profiles for x=(2n+1)h (n=0, 1, ... 4).

C. Optical Path Distortion Analysis

Designers of optical systems are interested in the RMS of the optical path difference (OPD_{rms}, Eq. 16), which was computed from the instantaneous OPD (Eq. 15) for an aperture that extends from $x = 12.3mm$ to $x = 63.3mm$ ($2.5 \leq x/h \leq 12.7$). Instantaneous visualizations of the OPD in Fig. 17 reveal high optical distortions for case T1S2 ($He, T_0 = 300K$).

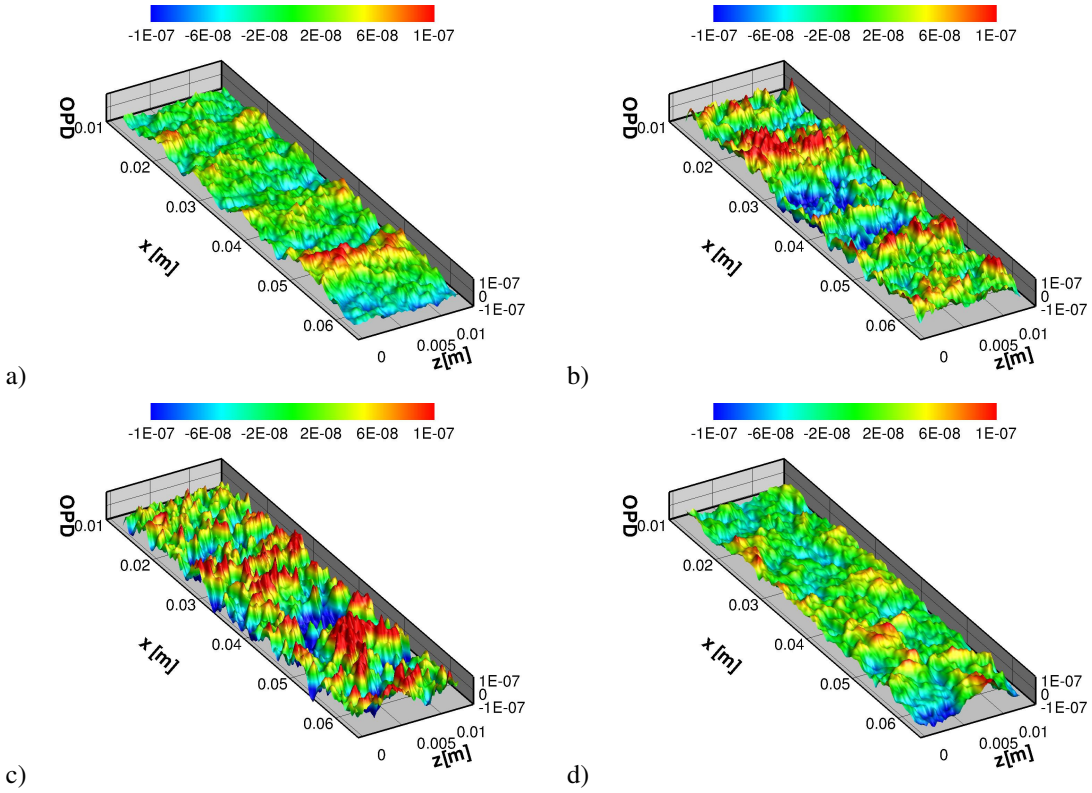

Fig. 17 Instantaneous OPD (in m) for a) T1S1, b) T2S1, c) T1S2 and d) T2S2.

In Fig. 18, the normalized cumulative contribution to the OPD_{rms},

$$\Phi(y) = \frac{OPD_{rms}|_0^y}{OPD_{rms}|_0^\infty}, \tag{20}$$

for the different cases is compared. Also included in the figure, is the rate of change, $d\Phi/d(y/h)$, which reveals where contribution to the OPD_{rms} occurs. For case T1S1 (CO_2, $T_0 = 300K$), the $d\Phi/d(y/h)$ curve has a weak maximum near $y/h = 1$ and a slow decrease in the contribution near $y/h = 2$. The latter is attributed to optical distortions caused by the separated turbulent boundary layer. For case T2S1 (CO_2, $T_0 = 650K$), in agreement with the much larger density fluctuations (Fig. 16), a pronounced mixing layer peak is observed at $y/h = 0.8$. For this case, the near wall density fluctuations also make a significant contribution to the OPD. Concerning the He cases, for both total temperatures the $d\Phi/d(y/h)$ mixing layer peak is near $y/h = 1$. With increasing total temperature, the mixing layer contribution decreases and the boundary layer contribution increases. In general, the OPD contributions (Fig. 18) are fairly well aligned with the density fluctions (Fig. 16) suggesting a direct connection between the two.

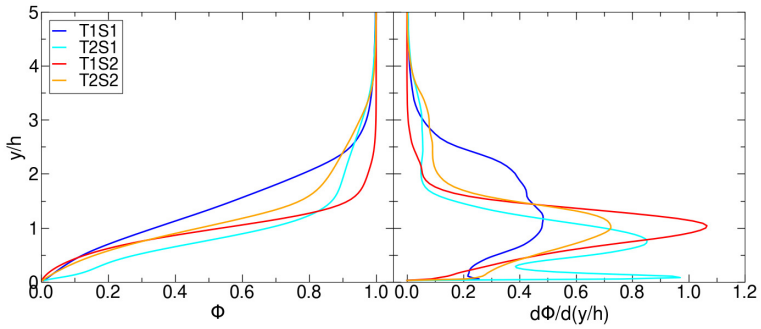

Fig. 18 Normalized cumulative contribution to OPD_{rms}, Φ, and rate of change, $d\Phi/dy$, as function of wall-normal distance for aperture of 2.5≤x/D≤12.7.

Table 7 provides the OPD_{rms} values obtained from the ND experiments [34, 35] and simulations. Concerning the simulations, for the CO_2 cooling gas cases the optical distortions increase with tunnel total temperature. The opposite trend is observed for the He cases in both experiments and simulations. By far the largest optical distortions are obtained for case T1S2 ($He, T_0 = 300K$). While helium provides effective wall cooling (see Fig. 11), the large optical distortions are undesirable.

Table 7 Levels of aero-optical distortions for both the experiments and the simulations, quantified by OPD_{rms} (in μm).

Case	T1S1	T2S1	T1S2	T2S2
Experiments	0.0413	0.0344	0.0544	0.0316
Simulations	0.03045	0.05201	0.07393	0.03733

D. Proper Orthogonal Decomposition

A total of 500 snapshots of the density field for $0mm < x < 173mm$ ($0 \leq x/h \leq 34.6$), equally distributed over a time interval of one, were analyzed with the POD. The eigenvalue spectra are compared in Fig. 19a. Consistent with the low RMS density fluctuations in Fig. 16, the eigenvalues are smallest for case T1S1. For all cases, a significant drop of the eigenvalue value magnitude is observed over the first 10 modes, suggesting that the lower modes contribute strongly to the density fluctuations and thus the optical distortions.

Figure 19b provides the time-coefficients for modes 1 and 3. For cases T1S1, T2S1, and T2S2, modes 1 & 2 and 3 & 4 form pairs with similar eigenvalue magnitudes as well as time-coefficients and mode shapes that are similar and shifted by a quarter wavelength with respect to each other. Such mode pairs capture traveling waves. Mode 1 has a noticeably longer period than mode 3. For case T1S2, the mode 3 period is much longer than the mode 1 period.

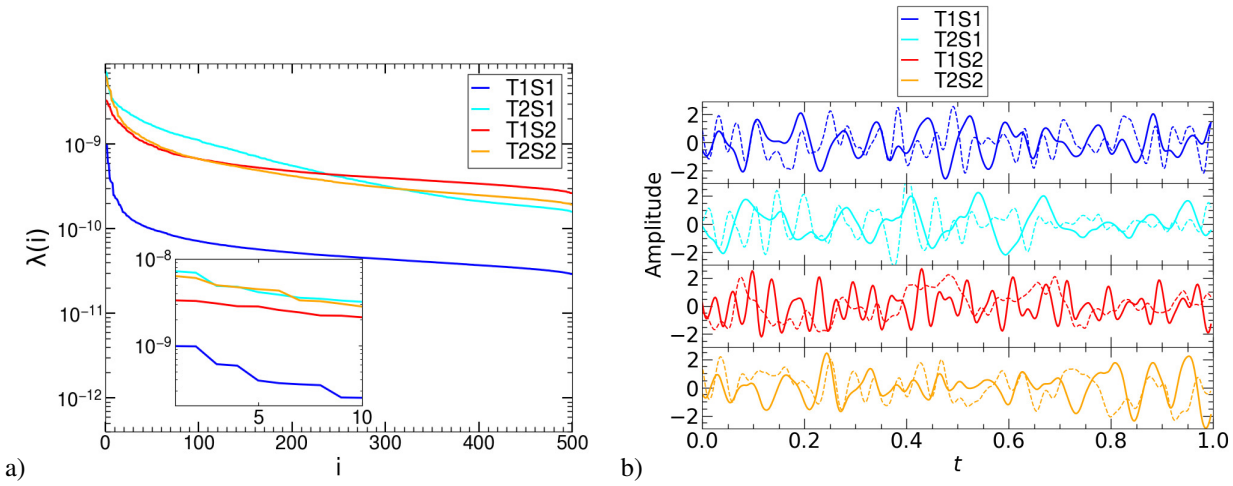

Fig. 19 Proper orthogonal decomposition a) eigenvalues and b) time coefficients (——, mode 1, - - -, mode 3).

Visualizations of modes 1 and 3 are provided in Fig. 20. For the $T_0 = 650K$ cases, the velocity difference across the mixing layer is large (see Fig. 10a), giving rise to strong mixing layer structures. For case T2S1, the mode 3 mixing layer structures are spanwise coherent and similar to those reported by Brown and Roshko [2] for turbulent mixing layers. For case T1S1, the POD structures are less coherent and appear more related to the approach boundary layer, although mode 3 captures spanwise coherent structures for the downstream part of the mixing layer. However, the POD mode amplitudes are low and the modes are noisy. For case T1S2, the POD captures oblique (mode 1) and streamwise (mode 3) mixing layer structures. This case has the largest density difference across the mixing layer (see Fig. 10c) and the largest OPD_{rms}-value (Tab. 7).

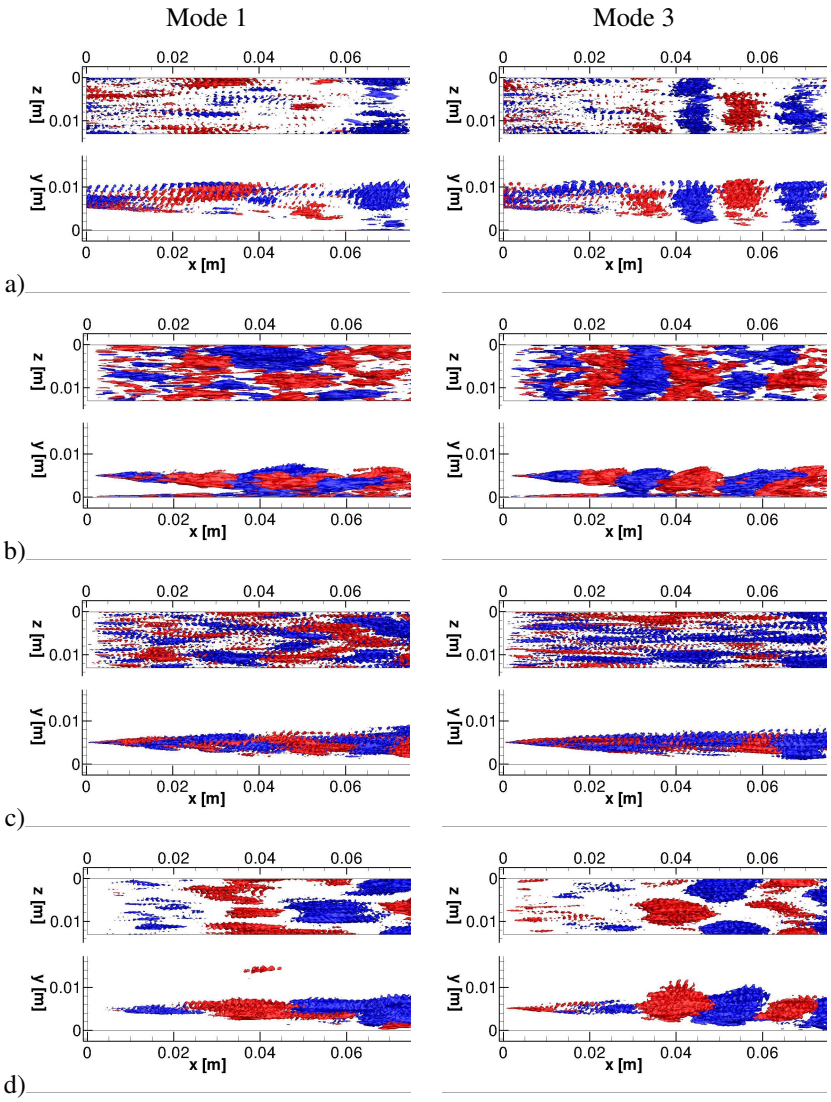

Fig. 20 Density iso-surfaces for POD modes 1 (left) and 3 (right) for a) T1S1 ($\rho = \pm 0.004$), b) T2S1 ($\rho = \pm 0.025$), c) T1S2 ($\rho = \pm 0.01$) and d) T2S2 ($\rho = \pm 0.015$).

In Fig. 21, the normalized cumulative POD eigenvalue magnitude,

$$\frac{\sum_{j=1}^{i} \lambda_j}{\sum_{j=1}^{300} \lambda_j}, \tag{21}$$

and normalized cumulative contribution of the POD modes to the OPD_{rms} are plotted versus the mode number. The first 10 modes capture 5% (case T1S2) to 10% (case T1S1) of the total eigenvalue magnitude. Interestingly, the contribution of the first 10 modes to the OPD_{rms} is much higher (up to 46% of the total OPD_{rms}). For cases T2S1 and T2S2, the first five modes make a particularly strong contribution to the OPD_{rms} (33% and 40%, respectively). These are the same cases for which the leading POD modes capture well-defined coherent structures (Fig. 20).

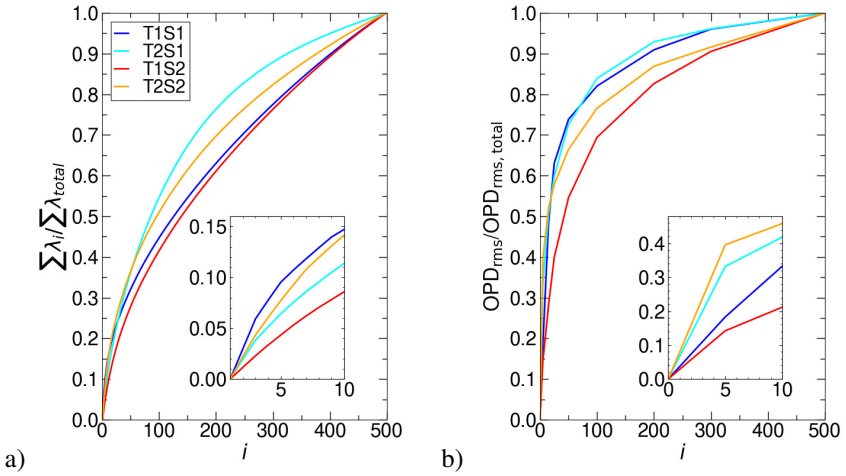

Fig. 21 Cumulative a) POD eigenvalue magnitude and b) OPD_{rms}.

IV. Conclusions

Film cooling of optical windows on hypersonic flight vehicles is often used to shield the window from damaging heat. A highly turbulent mixing layer, that develops at the interface between the freestream flow and cooling film, introduces significant density fluctuations, which in turn will create spatially and temporally varying optical distortions. To quantify the fluidic and aero-optical environment created by the mixing layer, wall-modeled large-eddy simulations (WMLES) for canonical two-dimensional cooling film flows over an optical window at supersonic (Mach 2) freestream conditions were performed. The simulations provide physical insight into the origin of the aero-optical distortions and, along with complimentary experimental results, they also provide data for the development of a model to predict the optical distortions for the supersonic flight regime [33]. Previous WMLES with air as a cooling gas species were presented and discussed by Torres Andrade et al. [37]. The present work focuses on the effect of the cooling film gas (i.e., cooling film gases that are species-mismatched with the air freestream) on the time-averaged levels of the aero-optical distortions, expressed as OPD_{rms} values. Specifically, carbon dioxide (CO_2) and helium (He) were considered in the simulations. The freestream total temperature for the simulations was $T_0 = 300K$ and $650K$. For the higher total temperature, the freestream is faster and less dense. It is shown that both the velocity gradient and density gradient across the mixing layer affect the root-mean-square (RMS) of the density fluctuations, which directly feed into the OPD_{rms}. While the former increases the turbulent shear stress, the latter leads to more baroclinic torque vorticity production. For helium, the adiabatic wall temperature for $T_0 = 650K$ is lower, suggesting better cooling of the optical window. The RMS of the density fluctuations and the OPD_{rms} are largest for CO_2 at $T_0 = 650K$ and He at $T_0 = 300K$. While for the former this can be explained by the highly turbulent mixing layer, for the latter it can be attributed to a large density gradient across the mixing layer. A proper orthogonal decomposition (POD) with density-based kernel was performed to isolate the coherent structures that contribute most to the OPD_{rms}. For all cases, streamwise coherent structures contribute chiefly

to the OPD_{rms}. For the cases with large velocity and density gradient across the mixing layer, spanwise coherent flow structures also contribute to the OPD_{rms}. For the CO_2 and He cooling films at a freestream stagnation temperature of $T_0 = 650K$, the leading five POD modes contribute significantly to the OPD_{rms}. For the latter case, the OPD_{rms} is considerably lower and the wall cooling is better. Flow control aimed at breaking up the dominant coherent structures can likely reduce the optical distortions even further. The present results suggest that faster cooling gas injection would lower the velocity gradient across the mixing layer and hence the turbulent shear stress. Alternatively, by matching the cooling film and freestream density, the baroclinic torque vorticity production can be reduced. Depending on the external flow environment, the cooling film gas has to be carefully selected to assure both effective wall cooling and low optical distortions.

V. Acknowledgement

This research was funded by the Office of Naval Research (ONR) under grant number N00014-22-1-2454 with Dr. Eric Marineau serving as program manager. High Performance Computing (HPC) resources were provided by the Department of Defense HPC Modernization Program.

References

[1] Yi, S., Ding, H., Luo, S., Sun, X., and Xia, Z., "Research progress on aero-optical effects of hypersonic optical window with film cooling," *Light: Science & Applications*, Vol. 13, No. 1, 2024, p. 310. https://doi.org/10.1038/s41377-024-01596-x.

[2] Brown, G. L., and Roshko, A., "On density effects and large structure in turbulent mixing layers," *Journal of Fluid Mechanics*, Vol. 64, No. 4, 1974, pp. 775–816. https://doi.org/10.1017/S002211207400190X.

[3] Papamoschou, D., and Roshko, A., "The compressible turbulent shear layer: an experimental study," *Journal of fluid Mechanics*, Vol. 197, 1988, pp. 453–477. https://doi.org/10.1017/S0022112088003325.

[4] Dimotakis, P. E., "Turbulent free shear layer mixing and combustion," Tech. Rep. FM91-2, Graduate Aeronautical Laboratories, California Institute of Technology, 1991.

[5] Rossmann, T., "An experimental investigation of high-compressibility mixing layers," Ph.D. thesis, Stanford University, 2002.

[6] Tan, J., Zhang, D., and Lv, L., "A review on enhanced mixing methods in supersonic mixing layer flows," *Acta Astronautica*, Vol. 152, 2018, pp. 310–324. https://doi.org/10.1016/j.actaastro.2018.08.036.

[7] Huang, W., "Mixing enhancement strategies and their mechanisms in supersonic flows: A brief review," *Acta Astronautica*, Vol. 145, 2018, pp. 492–500. https://doi.org/10.1016/j.actaastro.2018.02.022.

[8] Ao, W., Chen, Z., Liu, P., Shang, S., Ma, K., and Fu, B., "Mixing enhancement in a subsonic-supersonic shear layer with a cavity splitter plate," *Aerospace Science and Technology*, Vol. 102, 2020, p. 105847. https://doi.org/10.1016/j.ast.2020.105847.

[9] Goebel, S. G., and Dutton, J. C., "Experimental study of compressible turbulent mixing layers," *AIAA Journal*, Vol. 29, No. 4, 1991. https://doi.org/10.2514/3.10617.

[10] Zhao, Y., Yi, S., Tian, L., and Cheng, Z., "Supersonic flow imaging via nanoparticles," *Science in China Series E: Technological Sciences*, Vol. 52, 2009, pp. 3640–3648. https://doi.org/10.1007/s11431-009-0281-3.

[11] Tan, J., Zhang, D., Li, H., and Hou, J., "Detailed experimental investigations on flow behaviors and velocity field properties of a supersonic mixing layer," *Acta Astronautica*, Vol. 144, 2018, pp. 30–38. https://doi.org/10.1016/j.actaastro.2017.12.010.

[12] Goldstein, R. J., "Film cooling," *Advances in heat transfer*, Vol. 7, Elsevier, 1971, pp. 321–379. https://doi.org/10.1016/S0065-2717(08)70020-0.

[13] Majeski, J., and Weatherford, R., "Development of an empirical correlation for film-cooling effectiveness," *23rd Thermophysics, Plasmadynamics and Lasers Conference*, 1988, p. 2624. https://doi.org/10.2514/6.1988-2624.

[14] Richards, B., and Stollery, J., "Laminar film cooling experiments in hypersonic flow," *Journal of Aircraft*, Vol. 16, No. 3, 1979, pp. 177–181. https://doi.org/10.2514/3.58502.

[15] Kwok, F., Andrew, P., Ng, W.-F., and Schetz, J., "Experimental investigation of a supersonic shear layer with slot injection of helium," *AIAA journal*, Vol. 29, No. 9, 1991, pp. 1426–1435. https://doi.org/10.2514/3.10756.

[16] Juhany, K., Hunt, M., and Sivo, J., "Influence of Injectant Mach Number and Temperature on Supersonic Film Cooling," *Journal of Thermophysics and Heat Transfer*, Vol. 8, No. 1, 1994, pp. 59–67. https://doi.org/10.2514/3.501.

[17] Auvity, B., Etz, M. R., and Smits, A. J., "Effects of transverse helium injection on hypersonic boundary layers," *Physics of Fluids*, Vol. 13, No. 10, 2001, pp. 3025–3032. https://doi.org/10.1063/1.1401813.

[18] Konopka, M., Meinke, M., and Schröder, W., "Large-Eddy Simulation of Shock-Cooling-Film Interaction at Helium and Hydrogen Injection," *Physics of Fluids*, Vol. 25, No. 10, 2013. https://doi.org/10.1063/1.4823745.

[19] Peter, J. M., and Kloker, M. J., "Direct numerical simulation of supersonic film cooling by tangential blowing," *High Performance Computing in Science and Engineering'19: Transactions of the High Performance Computing Center, Stuttgart (HLRS) 2019*, Springer, 2021, pp. 263–278. https://doi.org/10.1007/978-3-030-66792-4_18.

[20] Mi, Q., Yi, S., Zhao, X., Zhang, B., and Lu, X., "Experimental study on cooling efficiency of hypersonic optical window," *Journal of Applied Fluid Mechanics*, Vol. 15, No. 1, 2021, pp. 63–72. https://doi.org/10.47176/jafm.15.01.32617.

[21] Sun, X., Ding, H., Liu, M., Yi, S., and Zhao, Y., "Experimental investigation on supersonic film cooling of hypersonic optical dome under different nozzle pressure ratios," *Aerospace Science and Technology*, Vol. 140, 2023, p. 108488. https://doi.org/10.1016/j.ast.2023.108488.

[22] Sun, X., Ding, H., Yi, S., Liu, M., and Huo, J., "Research on supersonic film cooling of hypersonic optical window under different nozzle pressure ratios," *Physics of Fluids*, Vol. 36, No. 10, 2024. https://doi.org/10.1063/5.0230116.

[23] Xia, Z., Ding, H., and Yi, S., "Inhibition of the aero-optical effects of supersonic mixing layers based on the RVGAs' control," *Chinese Optics Letters*, Vol. 21, No. 3, 2023, p. 030102. https://doi.org/10.3788/COL202321.030102.

[24] Sun, X., Ding, H., Liu, M., and Yi, S., "Supersonic film cooling improvement of hypersonic optical dome using microvortex generators," *AIAA Journal*, Vol. 62, No. 4, 2024, pp. 1626–1631. https://doi.org/10.2514/1.J063256.

[25] Ayyalasomayajula, H., Arunajatesan, S., Kannepalli, C., and Sinha, N., "Large Eddy Simulation of a Supersonic Flow Over a Backward-Facing Step For Aero-Optic Analysis," *AIAA Paper 2006-1416*, 2006. https://doi.org/10.2514/6.2006-1416.

[26] Su, C., "Aero-optical analysis of a film-cooled optical window based on linear stability analysis," *AIAA Journal*, Vol. 57, No. 7, 2019, pp. 2840–2850. https://doi.org/10.2514/1.J058150.

[27] Ding, H., Yi, S., and Zhao, X., "Experimental investigation of aero-optics induced by supersonic film based on near-field background-oriented schlieren," *Applied Optics*, Vol. 58, No. 11, 2019, pp. 2948–2962. https://doi.org/10.1364/AO.58.002948.

[28] Guo, G., Tong, X., and Luo, Q., "Numerical Investigation on Image Degradation Caused by Aero-Optical Effects of the Supersonic Mixing Layer," *Applied Optics*, Vol. 59, No. 35, 2020. https://doi.org/10.1364/AO.409548.

[29] Yao, X., Hao-Lin, D., Bo, Z., and Shi-He, Y., "Experimental investigation on the aero-optical effects of supersonic gas films with various cooling fluids," *Applied Optics*, Vol. 62, No. 32, 2023, pp. 8614–8620. https://doi.org/10.1364/AO.504090.

[30] Ding, H., Yi, S., Zhao, X., Xiong, H., and Ouyang, T., "Experimental investigation on aero-optical mitigation of hypersonic optical dome using microvortex generators," *Aiaa Journal*, Vol. 57, No. 6, 2019, pp. 2653–2658. https://doi.org/10.2514/1.J058084.

[31] Patel, T. K., Hess, A., Lin, D., Herndon, M., and Kessler, D. A., "Numerical Simulation of the Aero-Optical Distortion in 3D Compressible Turbulent Shear Layers," *AIAA SCITECH 2024 Forum*, 2024. https://doi.org/10.2514/6.2024-1030.

[32] Fassler, A., Leonov, S., and Gordeyev, S., "Optical effects of a temperature-mismatched supersonic mixing layer," *Unconventional Imaging, Sensing, and Adaptive Optics 2023*, Vol. 12693, SPIE, 2023, pp. 383–396. https://doi.org/10.1117/12.2677429.

[33] Fassler, A., Leonov, S., and Gordeyev, S., "Optical Effects of a Temperature-Mismatched and Species-Mismatched Supersonic Mixing Layer," *AIAA Paper 2024-1027*, 2024. https://doi.org/10.2514/6.2024-1027.

[34] Fassler, A., Leonov, S., and Gordeyev, S., "Optical and thermal effects of a species-mismatched supersonic mixing layer formed over a cooled optical window," *Unconventional Imaging, Sensing, and Adaptive Optics 2024*, Vol. 13149, SPIE, 2024, pp. 85–102. https://doi.org/10.1117/12.3027742.

[35] Fassler, A., Gordeyev, S., and Leonov, S. B., "Optical Studies of a Supersonic Mixing Layer Using a Convergent-Divergent Beam Approach," *AIAA Paper AIAA-2025-2768*, 2025. https://doi.org/10.2514/6.2025-2768.

[36] Andrews, P., Lax, P., Elliott, S., Firsov, A., and Leonov, S., "Flow Characterization at Heated Air Supersonic Facility SBR-50," *Fluids*, Vol. 7, No. 5, 2022. https://doi.org/10.3390/fluids7050168.

[37] Torres Andrade, J., Castillo Gomez, P., Gross, A., Fassler, A., Leonov, S., and Gordeyev, S., "Numerical Simulations and Aero-Optical Analysis of Temperature-Mismatched Supersonic Mixing Layers," *AIAA Journal - accepted for publication*, 2026.

[38] Lumley, J. L., "The structure of inhomogeneous turbulent flows," *Atmospheric Turbulence and Radio Wave Propagation*, 1967, pp. 166–178.

[39] Sirovich, L., "Turbulence and the dynamics of coherent structures Part I: Coherent Structures," *Quarterly of Applied Mathematics*, Vol. 45, No. 3, 1987, pp. 561–571. URL https://www.jstor.org/stable/43637457.

[40] Gross, A., and Fasel, H., "High-Order Accurate Numerical Method for Complex Flows," *AIAA Journal*, Vol. 46, No. 1, 2008, pp. 204–214. https://doi.org/10.2514/1.22742.

[41] Ahmed, A., and Gross, A., "Development & Testing of Thermo-Chemical Non-Equilibrium Extension for Large Eddy Simulation Code," *AIAA AVIATION FORUM AND ASCEND 2024*, 2024, p. 4369. https://doi.org/10.2514/6.2024-4369.

[42] Balsara, D., Garain, S., and Shu, C. W., "An Efficient Class of WENO Schemes with Adaptive Order," *Journal of Computational Physics*, Vol. 326, 2016, pp. 780–804. https://doi.org/10.1016/j.jcp.2016.09.009.

[43] Nicoud, F., and Ducros, F., "Subgrid-Scale Stress Modelling Based on the Square of the Velocity Gradient Tensor," *Flow, Turbulence and Combustion*, Vol. 62, No. 3, 1999, pp. 183–200. https://doi.org/10.1023/A:1009995426001.

[44] Bell, I. H., Wronski, J., Quoilin, S., and Lemort, V., "Pure and Pseudo-pure Fluid Thermophysical Property Evaluation and the Open-Source Thermophysical Property Library CoolProp," *Industrial & Engineering Chemistry Research*, Vol. 53, No. 6, 2014, pp. 2498–2508. https://doi.org/10.1021/ie4033999, URL http://pubs.acs.org/doi/abs/10.1021/ie4033999.

[45] Engineering ToolBox, 2024. URL https://www.engineeringtoolbox.com/air-diffusion-coefficient-gas-mixture-temperature-d_2010.html.

[46] Gross, A., and Fasel, H. F., "Multi-block Poisson grid generator for cascade simulations," *Mathematics and Computers in Simulation*, Vol. 79, No. 3, 2008, pp. 416–428. https://doi.org/10.1016/j.matcom.2008.01.042.

[47] Gross, A., and Fasel, H., "Characteristic ghost cell boundary condition," *AIAA journal*, Vol. 45, No. 1, 2007, pp. 302–306. https://doi.org/10.2514/1.23130.

[48] Stolz, S., and Adams, N., "Large-Eddy Simulation of High-Reynolds-Number Supersonic Boundary Layer using the Approximate Deconvolution Model and a Rescaling and Recycling Technique," *Physics of Fluids*, Vol. 15, No. 8, 2003, pp. 2398–2412. https://doi.org/10.1063/1.1588637.

[49] Gladstone, J., and Dale, T., "Researches on the Refraction, Dispersion, and Sensitivities of Liquids," *Philosophical Transactions of the Royal Society of London*, Vol. 153, 1863, pp. 317–343.

[50] Merzkirch, W., *Flow Visualization*, 2nd ed., Academic Press, 2012.

[51] Clergent, Y., Durou, C., and Laurens, M., "Refractive Index Variations for Argon, Nitrogen and Carbon Dioxide at λ = 632.8nm (He-Ne Laser Light) in the Range 288.15 ≤ T ≤ 323.15 K, 0 < p < 110 kPa," *Journal of Chemical & Engineering Data*, Vol. 44, 1999, pp. 197–199. https://doi.org/10.1021/je980133o.

[52] Mackey, L. E., and Boyd, I. D., "Assessment of hypersonic flow physics on aero-optics," *AIAA Journal*, Vol. 57, No. 9, 2019, pp. 3885–3897. https://doi.org/10.2514/1.J057869.

[53] Mansfield, C. R., and Peck, E. R., "Dispersion of helium," *Journal of the Optical Society of America*, Vol. 59, No. 2, 1969, pp. 199–204. https://doi.org/10.1364/JOSA.59.000199.

[54] Taira, K., Brunton, S. L., Dawson, S. T., Rowley, C. W., Colonius, T., McKeon, B. J., Schmidt, O. T., Gordeyev, S., Theofilis, V., and Ukeiley, L. S., "Modal analysis of fluid flows: An overview," *AIAA Journal*, Vol. 55, No. 12, 2017, pp. 4013–4041. https://doi.org/10.2514/1.J056060.

[55] Cheng, Y., and Chen, Q., "Large eddy simulation and dynamic mode decomposition of turbulent mixing layers," *Applied Sciences*, Vol. 11, No. 24, 2021, p. 12127. https://doi.org/10.3390/app112412127.

[56] Yule, A. J., *Two-dimensional self-preserving turbulent mixing layers at different free stream velocity ratios*, HM Stationery Office, 1971.

[57] Patel, R. P., "An experimental study of a plane mixing layer," *AIAA Journal*, Vol. 11, No. 1, 1973, pp. 67–71. https://doi.org/10.2514/3.6671.

[58] Miles, J. B., and Shih, J.-s., "Similarity parameter for two-stream turbulent jet-mixing region," *AIAA Journal*, Vol. 6, No. 7, 1968, pp. 1429–1430. https://doi.org/10.2514/3.4782.